

Excitation of the centrifugally driven interchange instability in a plasma confined by a magnetic dipole^{a)}

B. Levitt,^{b)} D. Maslovsky, M. E. Mael, and J. Waksman
*Department of Applied Physics and Applied Mathematics, Columbia University,
 New York, New York 10027*

(Received 22 November 2004; accepted 27 January 2005; published online 5 May 2005)

The centrifugally driven electrostatic interchange instability is excited for the first time in a laboratory magnetoplasma. The plasma is confined by a dipole magnetic field, and the instability is excited when an equatorial mesh is biased to induce a radial current that creates rapid axisymmetric plasma rotation. The observed instabilities appear quasicohherent in the lab frame of reference; they have global radial mode structures and low azimuthal mode numbers, and they are modified by the presence of energetic, magnetically confined electrons. The mode structure is measured using a multiprobe correlation technique as well as a novel 96-point polar imaging diagnostic which measures particle flux along field lines that map to the pole. Interchange instabilities caused by hot electron pressure are simultaneously observed at the hot electron drift frequency. Adjusting the hot electron fraction α modifies the stability as well as the structures of the centrifugally driven modes. In the presence of larger fractions of energetic electrons, $m=1$ is observed to be the dominant mode. For faster rotating plasmas containing fewer energetic electrons, $m=2$ dominates. Results from a self-consistent nonlinear simulation reproduce the measured mode structures in both regimes. The low azimuthal mode numbers seen in the experiment and simulation can also be interpreted with a local, linear dispersion relation of the electrostatic interchange instability. Drift resonant hot electrons give the instability a real frequency, inducing stabilizing ion polarization currents that preferentially suppress high- m modes. © 2005 American Institute of Physics.
 [DOI: 10.1063/1.1888685]

I. INTRODUCTION

Interchange instabilities occur in a variety of natural and artificial situations, including the gravitational Rayleigh–Taylor instability found in the F -layer of the ionosphere¹ and the pressure-driven interchange instability found in magnetic confinement configurations.² The interchange instability mixes plasma while minimizing changes in the magnetic field, and its nonlinear evolution causes plasma transport. For example, curvature-driven interchange instabilities in plasmas confined by shear-free magnetic fields were observed in the outer region of multipoles³ and, more recently, in steady current-free plasma discharges created in a purely toroidal magnetic field. In the later case, the structure of the interchange mode evolved into a rotating electrostatic dipole vortex⁴ that transported mass, energy, and charge.⁵

The centrifugally driven interchange instability plays an especially important role in the Jovian magnetosphere since interchange mixing is likely to be the mechanism for outward transport of approximately one ton of ionized matter each second from I_o , an inner moon.^{6,7} Satellite measurements form a consistent estimate of the mean mass outflow velocity,⁸ and small “empty” flux tubes have been detected^{9,10} that may represent the buoyant, inward-moving return flux. Although the centrifugal interchange instability has been modeled theoretically^{11–13} and computationally,¹⁴

the spatial structures¹⁵ and particle interactions¹⁶ of centrifugal interchange dynamics are still poorly understood.

Although the centrifugal interchange has not been investigated in a laboratory plasma, the interchange driven by energetic electron pressure has been studied in detail,^{17–21} and the structure of the electrostatic mode documented.¹⁹ As will be described, energetic electrons influence the centrifugally driven interchange in the experiment. Energetic particles are also an important constituent in the magnetospheres of the gas giants. We characterize the structure of the centrifugal interchange instability with a parameter equal to the ratio of the ion centrifugal drift frequency ω_g to the magnetic drift frequency of the relevant energetic particles ω_{dh} . For a given ionic mass M_i and energetic electron energy E_h the ratio of the drift frequencies are $\omega_g/\omega_{dh} \propto (\frac{1}{2}M_i\omega_E^2L^2)/3E_h$, where L is the equatorial radius of the field line and ω_E is the azimuthal plasma rotation frequency. For the experiments described here, $\omega_g/\omega_{dh} \sim 1/100$ (using $E_h/M_i \sim 5$ keV/amu); whereas, the same ratio for Saturn is $1/55$; for Jupiter is $1/45$; and for Earth is 2×10^{-5} . (The Earth’s rotation is sufficiently slow that gravity dominates over the centrifugal force.) Although the plasma beta in our experiment is much lower than in either Jupiter’s or Saturn’s magnetosphere, we believe our findings of the electrostatic centrifugal interchange instability may be relevant to the dynamical processes of rapidly rotating giant magnetospheres.

Plasma rotation is known to excite instability. Apart from the centrifugal interchange instability, the magnetorota-

^{a)}Paper N12 3, Bull. Am. Phys. Soc. **49**, 250 (2004).

^{b)}Invited speaker. Electronic mail: bl187@columbia.edu

tional instability,²² thought to be important in differentially rotating stars and accretion disks, for example, is excited when magnetic fields destabilize differential rotation in electrically conducting flows. Parker instabilities and Kelvin–Helmholtz instabilities can also effect the stability of centrifugally confined plasmas.^{23–25}

Rotation is also important for its confinement properties. Efforts to use centrifugal forces from supersonic plasma rotation to modify magnetic confinement for thermonuclear fusion devices is under way.^{26,27} Stability depends largely on how rapidly the plasma is rotating and on the velocity shear of the rotation profile. Cross-field velocity shear can stabilize interchange modes in magnetized plasmas. We believe it is significant that in the observations reported here, the plasma rotation profile appears to have little or no shear and rotates rigidly.

In this paper, we report the first laboratory observation of the centrifugally driven interchange instability and its observed mode structure. The observations were made using a laboratory terrella device, the collisionless terrella experiment^{28–31,19–21} (CTX) that was modified with an axisymmetric tungsten mesh placed at the equator of the dipole electromagnet. When the mesh is negatively biased with respect to the outer vacuum vessel wall, the resulting radial current produces a rapid azimuthal plasma rotation and an outward centrifugal force on the plasma. Movable probes show the plasma has a nearly rigid azimuthal rotation and a steep radial density profile. Using a multiprobe correlation technique¹⁹ and a new polar imager array, the radial and azimuthal structures of the instability are measured and found to have long wavelengths comparable to the system size. Since the plasma contains a population of energetic, magnetically trapped electrons, the effects of collisionless, rapidly drifting particles are also studied. Both pressure-driven and centrifugal-driven interchange modes can occur during the same discharge but they modulate each other. Additionally, theoretical and numerical models suggest that these fast electrons explain the dominance of long wavelengths for the centrifugal instability observed in the laboratory.

The outline of this paper is as follows. Section II describes the CTX used to observe the centrifugal interchange instability. Here, we also describe the floating potential probe measurements and the frequency-domain correlation method used to reconstruct the radial, azimuthal, and field-aligned mode structure. The equatorial mesh used to bias the inner field lines with respect to the outer wall and spin up the plasma is also described, along with the rotating equilibrium established during negative bias. Section III summarizes the observations of the centrifugally driven interchange instability in a laboratory dipole plasma. The interaction of the modes with the hot electron instability is described as well as the multiprobe correlation analysis used to measure the instability mode structure. Section IV gives mode structure measurements from both the correlation technique and the polar imager. Low azimuthal modes are dominant and the harmonic components $m=1, 2,$ and 3 are described. The interchange mode is flutelike, radially broad, and rotates with a rigid spiral phase structure. Section V summarizes compari-

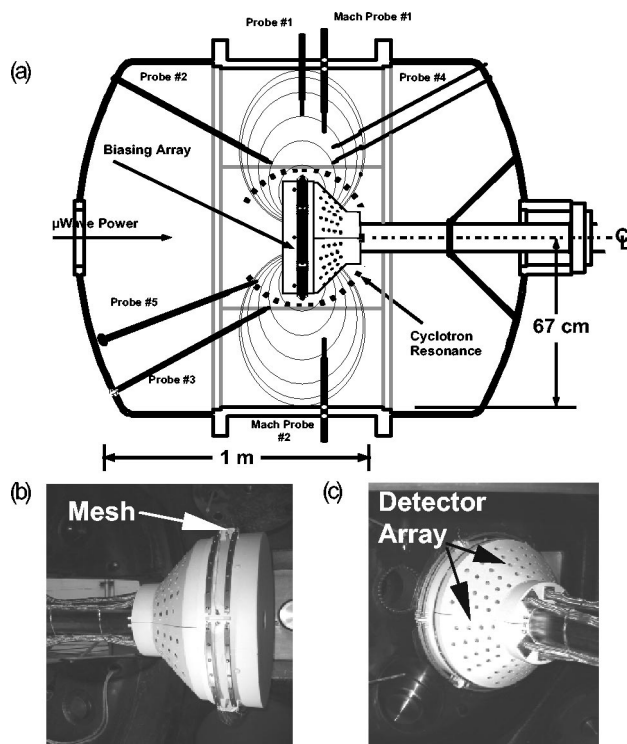


FIG. 1. (a) A schematic of the CTX vacuum chamber, depicting the magnetic field lines, equatorial mesh biasing array, several movable probes, and the polar current detector array. The location of the fundamental ECRH resonance is indicated by the dotted line. Photographs of the equatorial bias mesh (b) and the polar detector array (c) are also shown.

son of the experimental observations with linear theory and describes the self-consistent nonlinear simulation used to interpret the measurements. The small change to the simulation code, from that used in previous studies,¹⁹ needed to model the electrostatic centrifugal interchange is described. The simulation reproduces measurements of the radial mode structure, overall amplitude, and the observed effect of hot electrons. Finally, we summarize our results and describe some on-going efforts that will further investigate interchange motion in dipole magnetic fields.

II. EXPERIMENTAL METHODS

Figure 1(a) shows a schematic of the CTX device. The CTX plasma is produced with injection of 1 kW of 2.45 GHz microwave power. The electron cyclotron resonance heating (ECRH) and energetic electron production rate are known to be spatially localized near the fundamental cyclotron resonance at the dipole's equator. Typically, the microwave heating pulses last about 0.7 s, and the energetic electron pressure is adjusted by changing the background hydrogen gas pressure ($\sim 10^{-4}$ Pa). The CTX device consists of an ultra-high vacuum chamber, 140 cm in diameter, and a mechanically supported dipole electromagnet. A stainless steel enclosure electrically grounded to the chamber wall surrounds the magnet, which has a maximum magnetic field strength at the face of the terrella of 15 kG and decreases to 50 G at the vessel wall.

Electrostatic fluctuations are measured by five high impedance floating potential probes located at various positions

in the vacuum chamber. Each probe tip consists of a 1 mm stainless steel wire connected to a 100 k Ω resistor and 50 Ω coaxial cable contained within a ceramic tube. The fluctuating signals from the probe are amplified with impedance-matched wide-bandwidth amplifiers and digitized with high-speed, 8 bit digitizers. These probes can be repositioned radially to examine either potential fluctuations at different positions on the same field line or fluctuations on different field lines separated radially or separated azimuthally by 90° or 180°.

The tungsten filament bias-control system is an array of six tungsten meshes, distributed equatorially onto an insulating shell mounted onto the terrella. The meshes can be individually biased but in these studies only axisymmetric potentials were applied. A photograph of the biasing system is shown in Fig. 1(b). The bias cap itself is built from a spun stainless steel dish plasma-spray coated with 12 mil thickness of alumina to prevent current flow along field lines to the magnetic poles. Such a coating insulates to roughly 4–5 kV and is compatible with ultrahigh vacuum operation.

On the conical part of the insulated biasing cap sits a polar imaging diagnostic, shown in Fig. 1(c), which consists of 96 gridded particle detectors. The apertures for these detectors are 1 cm², and are distributed uniformly on a rectangular grid in the natural, magnetic flux coordinates (φ , ψ). The detector provides a good approximation to the bounce-averaged phase-space distribution F by measuring the flux of energetic electrons scattered to the poles as a result of electron-neutral collisions. The signal collected by the detectors is the particle flux integrated along flux tubes. Each signal is digitized by high-speed high-bandwidth transient recorders (1MHz, 14 bit) through transimpedance amplifiers. The detectors have three biasing grids as well as a current collector plate. The grids are typically biased at +500 V to repel ions, up to –2 kV to analyze the electron energy, and –9 V to suppress secondary electrons from the collector. The radial extent of the volume collected by the imaging diagnostic extends from the innermost flux surface to the outermost surface that does not contact the outer vacuum vessel.

A. Biased equilibrium

Upon application of a negative bias to the equatorial mesh array in the range of –100 to –600 V, significant modifications to the plasma equilibrium occur, as shown in Fig. 2. Floating potential measurements are plotted versus equatorial radius and show a clear increase from the unbiased case. The probes begin to destructively limit the plasma at around 45 cm, but we plot the inner boundary condition at the location of the bias array and infer that the potential increases up to this value. The equilibrium potential, Φ , has a $1/L$ dependence, where L defines the equatorial radial distance. The magnetic field is defined by the azimuthal angle, magnetic flux, and scalar potential, $\mathbf{B} = \nabla\varphi \times \nabla\psi = \nabla\chi$, and a constant $\mathbf{E} \times \mathbf{B}$ frequency, $\omega_E(\psi) = -\partial\Phi/\partial\psi$, of ~ 19 kHz across the plasma volume is calculated from the measured potential and the ideal dipole magnetic field, shown in Fig. 2(b). We note that the unbiased case shows a shear in the rotation profile as well as a reversal

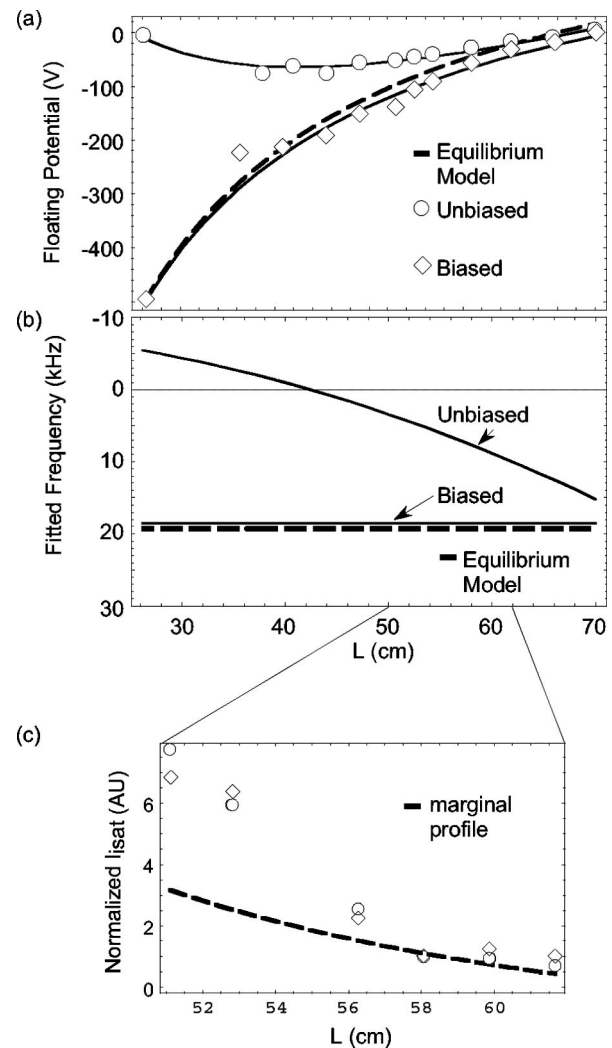


FIG. 2. (a) Floating potential measurements with and without external bias and (b) the $\mathbf{E} \times \mathbf{B}$ rotation frequency consistent with floating potential measurements. The dashed lines are model predictions based on classical Pedersen conductivity due to ion-neutral collisions. (c) Profile of the ion saturation current normalized to a fixed edge probe. The marginally stable density profile is indicated by the dotted line.

in the direction of plasma rotation. This reversal has also been confirmed with Mach probe measurement. Velocity shear is, in general, a stabilizing force for instabilities.²⁷

The equilibrium represented by the dashed lines in the top two plots is calculated from the requirement of constant radial current and Ohm's law, $\mathbf{J} = \sigma_p \mathbf{E}$, where $\sigma_p \approx nM_i v_{in}/B^2$ is the Pedersen conductivity, the radial cross-field conductivity caused by ion-neutral collisions, n is particle density number, M_i is ion mass, and v_{in} is the ion-neutral collision frequency, and shows close agreement with the profiles inferred from observation. The radial current is determined to be

$$I = 8\pi M_0 \Sigma_p \omega_E, \quad (1)$$

where Σ_p is the field-line integrated Pedersen conductivity,

$$\Sigma_p \equiv \frac{\int d\chi \sigma_p |\nabla \psi|^2 / B^2}{\int d\chi |\nabla \psi|^2 / B^2}, \quad (2)$$

and M_0 is the dipole magnetic moment. The current predicted from this model agrees with the measured current ~ 2 mA leading us to conclude that the ion current transport processes are near classical, driven by ion-neutral collisions. These measurements are also consistent with independent measurements of the plasma and neutral density n , which determines the ion-neutral collision frequency ν_{in} . Power on the order of 1–2 W is required to spin the plasma.

Biasing the equatorial array positively with respect to the vacuum chamber wall has also been studied, but positive bias does not cause plasma rotation in the region of the plasma accessible to probe measurements. This observation is similar to those by Saitoh and co-workers.³² In addition, the centrifugal modes that we describe in the following section are only observed with negative biases. This may be a result of the negative ambipolar potential of the unbiased plasma [see Fig. 2(a)] so that the application of a negative bias adds to the already negative space charge potential within the plasma. A positive bias, on the other hand, would subtract from the unbiased floating potential, creating two regions of oppositely directed electric fields. Most of the potential drop would appear across a limited region near the equatorial mesh. Positive bias results in a rotation profile with greater shear, which stabilizes interchange modes described here.

We also plot the ion saturation current normalized between one moving Langmuir probe and one stationary probe in Fig. 2(c). Ion saturation current is related linearly to density. Profiles of I_{isat} are compared in the presence and absence of the external bias, and both edge profiles are steep. Linear interchange theory requires an unstable density profile, $\partial N_0 / \partial \psi > 0$ (where N_0 is the particle number per unit magnetic flux¹⁹), which, for a dipole, is equivalent to an equatorial density profile $n(L)$ steeper than L^{-4} . Figure 2(c) also shows the marginally stable profile, indicating that both biased and unbiased profiles are clearly unstable.

III. OBSERVATION OF CENTRIFUGALLY DRIVEN MODES

When the equatorial mesh is biased sufficiently negatively, the plasma rotates rapidly and electrostatic fluctuations appear that we identify as the centrifugal interchange instability. The fluctuations are measured in the same way that was used to identify interchange instabilities driven by energetic electron pressure¹⁹ called the hot electron interchange instability, or HEI. We find the rotationally-driven fluctuations have very different characteristics, and are easily distinguishable from the instability driven by energetic electrons. The frequency is near (but slightly above) the plasma rotation rate ω_E (instead of the much faster magnetic drift frequency of the energetic electrons $\omega_{dh} \sim 0.5$ MHz); the amplitude of the fluctuations is 1–2 V (about 20–50 times smaller than the amplitude of the energetic electron inter-

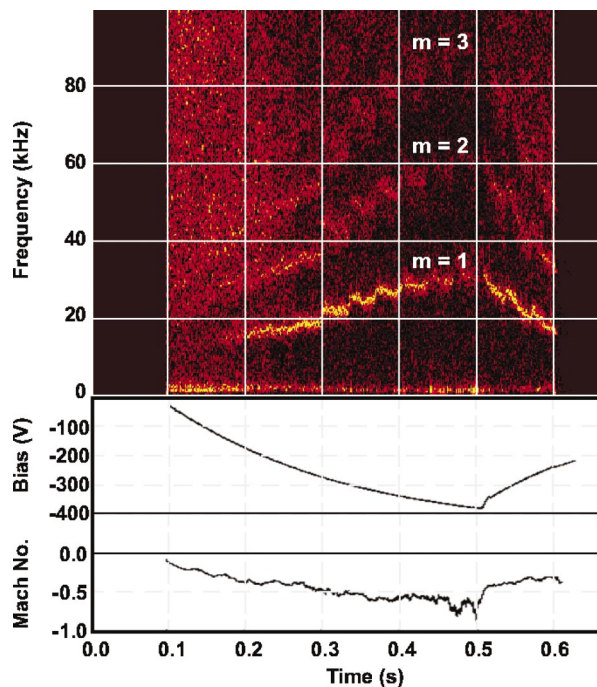


FIG. 3. (Color). Time-frequency spectrogram of interchange fluctuations upon application of mesh bias. Also shown is the Mach probe measurement of edge ion flow.

change); and the spectrum of the saturated instability evolves slowly as the equilibrium evolves (and periodic bursting is not observed). The most intense centrifugal instabilities occur as the density of the neutral gas is adjusted higher and when the strength of the magnetic dipole is lowered. Higher neutral density reduces the pressure of energetic electrons, thereby reducing the HEI instability drive, while simultaneously increasing the drive of the mass-driven centrifugal instability. Magnetic field reduction leads to faster rates of plasma rotation ω_E , which also increases the centrifugal drive.

Figure 3 shows probe measurements of the centrifugal instability from an individual experiment where the external bias on the equatorial mesh is ramped up from 0 V to more than -400 V. The azimuthal flow speed, as measured by a two-sided probe (i.e., a “Mach probe”), increases with the increasing external bias. In addition, electrostatic fluctuations measured by floating potential probes sampling at 200 kHz are observed upon application of the external bias, as the plasma spins up. The time-frequency domain spectrogram of the fluctuations is plotted, and increases in frequency with increasing external bias on the equatorial filaments. The lowest frequency mode is roughly 25 kHz, slightly above the calculated $\mathbf{E} \times \mathbf{B}$ frequency, with higher modes existing at integer multiples of the fundamental. Thus, a single nonsinusoidal mode is observed with smaller amplitude higher harmonics.

Figure 4 shows an interval during a discharge where the equatorial mesh increased from -250 V to -400 V. In this case, the magnetic field was reduced to 70% of its values from the example shown in Fig. 3. As the bias increases, the spectral characteristics and azimuthal structures of the fluc-

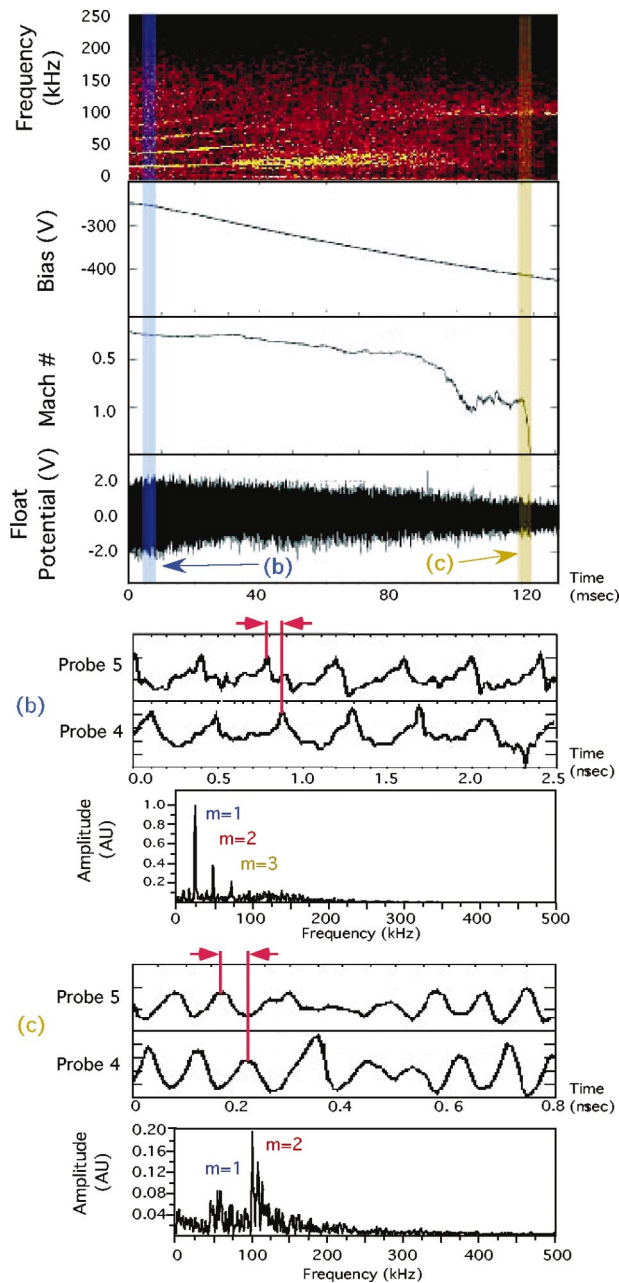


FIG. 4. (Color). Interchange fluctuations in plasmas with fastest rotation rates achieved by reducing the dipole magnetic field. When the applied mesh bias becomes more negative than -400 V, the interchange mode structure is dominated by $m=2$.

tuations evolve as measured by two probes separated by $\Delta\varphi=90^\circ$. At low bias, the lowest frequency mode is roughly 25 kHz, the same as shown in the previous figure, though the fluctuations shown are from a probe sampling at 1 MHz, instead of 200 kHz. As the bias level further increases, the azimuthal flow measured by the Mach probe shows a sharp increase $M\sim 1$ and the fluctuations transition to a higher frequency ~ 100 kHz and have a predominately $m=2$ azimuthal structure. The wave form of the fluctuations are shown with an expanded time scale in Figs. 4(b) and 4(c) as well as their normalized amplitude spectra. The direction of propagation can be obtained from the phase difference between the probes and confirms that the mode moves in the

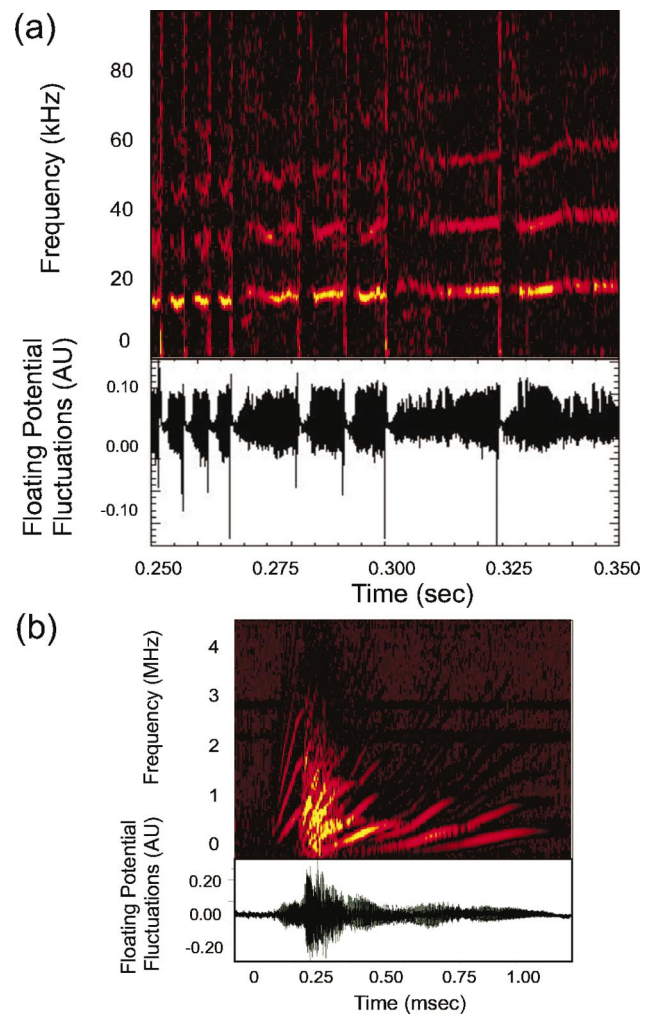


FIG. 5. (Color). Simultaneous observation of HEI and centrifugal modes during a low density shot. (a) The floating potential fluctuations and the corresponding time-frequency spectrograms are shown from one probe digitized at 200 kHz and (b) another probe sampling at 12.5 MHz displaying one of the HEI instability bursts, with their characteristic frequency sweeping.

$\mathbf{E} \times \mathbf{B}$ direction at ω_E . Probe scans across the plasma volume indicate that the mode is rigidly rotating with a constant angular frequency, consistent with the equilibrium model as shown in Fig. 2.

A. Interaction with HEI

When the fraction of hot electrons is large, then the HEI instability appears and the centrifugal instability is significantly modified. Bursts of HEI instability are observed which stabilize the centrifugal instability for several milliseconds. This is most likely because the pressure profile is flattened through HEI transport.^{20,21} Figure 5 shows the electrostatic potential fluctuations during several of these events; quasiperiodic HEI bursts are observed and repeatedly arrest the centrifugally driven fluctuations. Figure 5(b) shows fluctuations measured simultaneously with a high-speed digitizer and with a low-pass filter showing a single HEI burst. We also note the period of HEI bursts decreases as the bias increases. This is presumably because the centrifugal instabil-

ity also has a stabilizing effect on the HEI, causing longer periods required for the pressure profile to reach the stability threshold.¹⁷

Note that the HEI modes occur on the ω_{dh} time scale, in the ~ 1 MHz range. The HEI instability has been studied in detail in the CTX experiment.^{29-31,19-21} The interchange mode structure analysis performed in this paper for the rotational mode was previously accomplished for the HEI.¹⁹

B. Correlation analysis

The procedure for the correlation analysis has been described in detail previously.¹⁹ The complete electrostatic structure (i.e., azimuthal, radial, field-line structure, and mode amplitude profile) of the fluctuations can be obtained using this analysis. Five movable high impedance floating potential probes (with 100 k Ω tips) located at various positions within the plasma are used for the analysis. Cross-correlation analyses of combinations of probe pairs and a fixed “reference” probe yield mode structure information. The mode structure we present is that of the $m=1$ dominant region simply because its larger amplitude is easier to measure; mode structures of the $m=2$ region were measured and are qualitatively similar.

The radial coordinate for a field line is its equatorial distance L . Distance along a field line is labeled by s , and the azimuthal coordinate is φ . The measured probe position is mapped to its equivalent magnetic coordinate, $(L, \varphi, s) \rightarrow (M_0/\psi, \varphi, \int d\chi/B)$, by numerical computation. The quantities to be measured are expressed in terms of a modal prescription for the voltage measured by a probe located at (L, φ, s) ,

$$\Phi(L, \varphi, s, t) \equiv \sum_m \Re\{\Phi_m(L, t) \exp[i(m\varphi + k_L L - \omega_m t)]\}. \quad (3)$$

The amplitude, Φ_m changes slowly in time, but we find it does not change in spatial structure. We also find the $|\Phi|$ does not change significantly with s along a field line over the region accessible with the probes. These observations justify the modal prescription *a posteriori*.

When the digitized signals from two probes are Fourier transformed, the transform of the correlation between two probes $C(1, 2)$ is expressed as the product of one probe signal with the complex conjugate of the second. In terms of the modal prescription, this correlation is

$$C_{n,m}(1, 2) \approx \Phi_{n,m}(R_1) \Phi_{n,m}^*(R_2) \times \exp[i(m\Delta\varphi + k_{\parallel}\Delta s + k_R\Delta R)]. \quad (4)$$

Since $\Delta s = s_1 - s_2$ and $\Delta R = R_1 - R_2$ are known, the phase of the correlation can be used to determine m, k_{\parallel} , and k_R .

IV. MEASUREMENT OF GLOBAL MODE STRUCTURES

This section presents measurements of the global mode structure of the centrifugally driven interchange instability observed in the CTX device using two different methods,

with the multiprobe cross-correlation technique just discussed and with the polar imaging diagnostic described at the end of Sec. II.

A. Mode structure from multiprobe correlation

When two probes are located on the same field line, $\Delta\varphi = \Delta L = 0$, and the variation of the potential along the field line can be directly measured. Phases of the correlation function calculated between two such probes confirm the flutelike nature of the observed mode, and $k_{\parallel} \sim 0$ within the accuracy of measurements, $|k_{\parallel}\Delta s| < \pm 10^\circ$.

The azimuthal mode number shown in Figs. 4(b) and 4(c) is obtained from the phase of the correlation function of two probes separated only in azimuthal angle, i.e., $\Delta L \sim \Delta s \sim 0$, and $\Delta\varphi = 90^\circ$. As mentioned, the lowest frequency, largest amplitude mode in the low bias region is identified as the $m=1$ mode, with higher harmonics of gradually decreasing amplitude, while the higher bias region is characterized by a large $m=2$ mode.

The radial profiles of the amplitude and phase for the three lowest azimuthal components are shown in Figs. 6 and 7.

In Fig. 6, the radial profile of the normalized magnitude of the two-probe correlation function shows the radial structure to be broad and to depend on the azimuthal mode number, with lower m modes being broader generally. In all cases, the mode structure extends from the edge to the inner hot electron region, and they are not localized to particular flux surfaces (probes can only go in as far as the ECRH resonance location, whereupon their presence prevents plasma production). In addition, little time dependence is observed in these normalized profiles, although the relative amplitudes of one mode with another are observed to vary in time.

In Fig. 7, the phases of the three lowest m numbers are shown with each radial location representing averages of several shots having the movable probe at different positions. In Fig. 7(a) the dimensionless total phase $(m\Delta\varphi + k_L\Delta L)/2\pi$ is plotted versus radius. At roughly 55 cm both probes are at the same location, $\Delta L = 0$, where there is zero radial phase. Thus, the azimuthal mode number can be measured at this location (see dashed lines). Away from this location, nonzero radial phases are measured for all modes, contrary to the pressure driven modes which are characterized by $k_r \sim 0$.¹⁹ In Fig. 7(b) just the radial phase (computed by subtracting the azimuthal phase) of the $m=1$ mode is plotted in radians. A radial phase shift of nearly $\pi/2$ is seen between 55 cm and roughly 36 cm and is observed for all three modes, indicating a spiral radial structure for the electrostatic modes. Data are plotted for three different times and we observe no apparent time dependence in the phase. Fig. 7(c) shows a snap-shot of the $m=1$ mode as reconstructed from the probe data.

The mode structures of the centrifugal and HEI interchange modes, though driven by very different processes and on very different time scales, are surprisingly similar. It is perhaps the case that electrostatic flutelike modes in a dipole-confined plasma exhibit some universal characteristics relat-

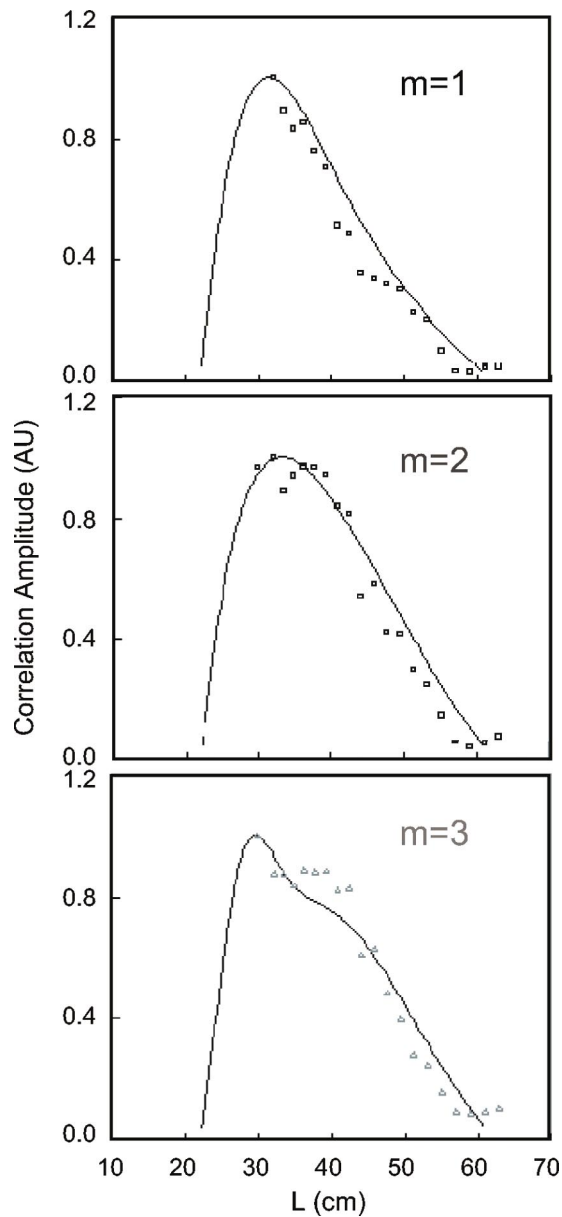


FIG. 6. Normalized magnitude of the correlation function between two probes as a function of the radial position of one probe for the $m=1, 2$, and 3 azimuthal components numbers. Solid lines are computed Fourier components from the nonlinear simulation.

ing to their global mode structures, notably their radial structures, time independence, and rigid rotation. The only major departure between the two cases is the radial phase structure: constant phase, independent of radius for HEI, and a spiral phase structure for the centrifugal mode.

B. Mode structure from polar diagnostic

In addition to obtaining the mode structure from the multiprobe correlation technique, it is possible to use the polar imaging array to obtain qualitatively similar results. The array consists of 96 detectors, comprising 8 radial positions and 24 azimuthal ones. In a single slowly evolving discharge, the entire mode structure can be observed as a function of time, in comparison with the probe correlation analysis (which requires many discharges with different

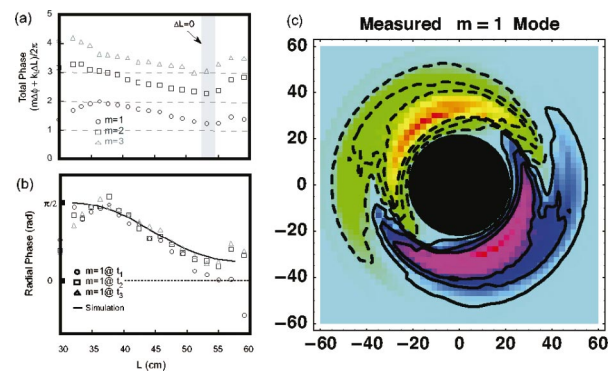


FIG. 7. (Color). (a) Total phase of the correlation function between two probes as a function of the radial position of one probe for the three lowest harmonics. (b) The radial phase for the $m=1$ mode at three different times during a discharge. Solid line is the result of numerical simulation. (c) Reconstructed $m=1$ component of the interchange mode.

probe locations). The polar array can also be used to construct video images of polar flux dynamics, as well as time averaged equilibrium and fluctuation contour plots, some examples of which are shown here. Interpolation for the contour plots was made using a quintic interpolation scheme.

Polar diagnostic data at each radial position, consisting of a given number of detectors, was Fourier decomposed and represented with $m=1-3$ modes. A singular value decomposition was performed to solve for the $\sin(m\phi)$ and $\cos(m\phi)$ coefficients of each mode, which determine the relative amplitudes and phases and the radial mode structure of the instability at the eight radial detector position. The phases, not shown here, indicate roughly rigid rotation at 25 kHz as well as some radial phase shift, similar to what was measured by the multiprobe correlation technique.

Since the centrifugal modes are quasicohherent, small time windows $\approx 100 \mu\text{s}$ were selected to make mode structure analyses. Averages over several oscillation periods are used for the presented data.

Figure 8 shows results from the polar imaging diagnostic, with detector positions mapped to the equatorial plane along field lines and marked by small circles. Again, results here are shown for the low bias $m=1$ dominated regime. A polar plot of the net polar electron current is shown in Fig. 8(a), with the equilibrium electron ring clearly visible. The fluctuations for the same discharge, Fig. 8(b), display a clear $m=1$ structure with some suggestion of the spiral structure alluded to previously; the dotted lines are contours of negative current, while the solid ones are of positive current. Figure 8(c) displays the relative amplitude frequency spectrum as measured by the polar imager; the resolution is blurred compared with Fig. 4(b) since the fast Fourier transform (FFT) time window sampled is small and also since it is an average of FFTs from all of the detectors; however, the dominant $m=1$ mode at ~ 25 kHz is clearly present. The normalized radial mode amplitude for the three lowest modes are also plotted in Fig. 8(d) and show qualitatively similar profiles to Fig. 6, with $m=1$ being the largest. As in the correlation analysis, higher m modes are seen to be broader and peaked at larger radii.

In comparing the mode structures from the two methods,

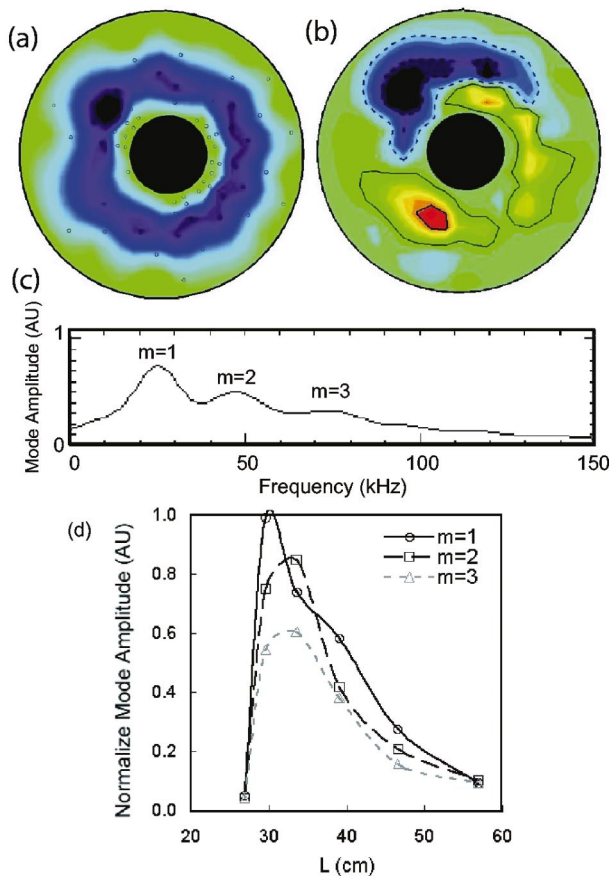


FIG. 8. (Color). Measurements using the polar imaging diagnostic. (a) Equilibrium and (b) fluctuations of the polar electron current. The small round circles indicate the detector locations in (a). (c) The frequency spectrum averaged over all detectors. (d) Radial profiles of the normalized amplitude for the three lowest azimuthal components of the fluctuating endloss current.

we note that they are derived from different fluctuation sources. The probe measurements describe the structure of the floating potential oscillations; whereas, the polar detector array measures fluctuations of the polar electron current.

V. COMPARISON WITH THEORY

To model our observations of the centrifugal mode and its complex interaction with hot electrons, comparison with both linear theory and a nonlinear simulation were undertaken. The linear dispersion relation of interchange instabilities driven by both pressure due to a distribution of hot electrons and centrifugal forces was derived in dipole flux coordinates. The nonlinear behavior of the combined interchange instabilities is studied by modifying a self-consistent numerical simulation originally written to study the HEI instability. In general, both methods find that short wavelengths are driven unstable by the purely rotational drive, while the HEI drive can excite different wavelength modes depending on the magnitude of the drive: for low drives, long wavelength modes are most unstable. This is the regime that is observed in all of the HEI and rotational mode studies. It is shown that finite temperature effects add a real frequency to the modes which induce polarization currents

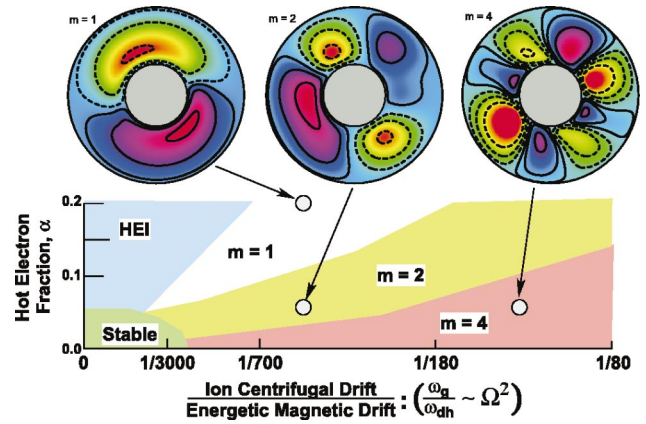


FIG. 9. (Color). Computed variation of the interchange mode structure as the fraction of energetic electrons α and the plasma rotation rate ω_E changes. Only the regimes dominated by $m=1$ and $m=2$ are seen experimentally.

which tend to stabilize higher m modes. The nonlinear simulation also reproduces the radial mode structure.

A. Linear theory

To facilitate the calculation of the linear dispersion relation, the following assumptions were made. Since microwave absorption at the electron cyclotron resonance only heats electrons, the ions are cold, and plasma pressure results from a fraction $\alpha(\psi)$ of energetic deeply-trapped electrons. The dipole magnetic field causes these energetic electrons to precess at a rate proportional to their kinetic energy $\omega_{dh} \propto \mu B / \psi$ with μ being the electron magnetic moment and an adiabatic invariant during slow interchange motion. Furthermore, since the trapped electrons have a distribution of energies $G(\mu)$ they create wave-particle resonances,²⁸ and interchange instabilities acquire a real frequency. The experimentally relevant (localized) linear dispersion relation³¹ for the interchange instability due to both centrifugal and pressure drives is

$$D(\omega, m) \approx 1 + \frac{m^2}{m_{\perp}^2} \left[\frac{\Gamma_g^2}{\omega^2} + \int d\mu \frac{\Gamma_h^2 G(\mu)}{\omega(\omega - m\omega_d)} \right], \quad (5)$$

where the centrifugal interchange rate Γ_g and the rate driven by trapped energetic electrons Γ_h are

$$\Gamma_g^2 = \omega_{ci} \omega_g \left(\frac{\psi}{N_i} \right) \frac{\partial N_i}{\partial \psi},$$

$$\Gamma_h^2 = 1.5 \omega_{ci} \omega_{dh}(\mu) \left(\frac{\psi}{N_i} \right) \frac{\partial(N_i \alpha)}{\partial \psi}.$$

The ratio m/m_{\perp} is the ratio of the azimuthal mode number to a dimensionless perpendicular wavelength, $m_{\perp}^2 \approx m^2 + 0.58(k_{\perp} L)^2$, that includes the radial variation of the mode structure. When $\alpha \rightarrow 0$, the centrifugal interchange is unstable whenever the particle number within a unit flux tube increases inward to the dipole magnet, $\partial N_i / \partial \psi > 0$ (or when the density profile is steeper than $n \propto 1/L^4$), as explained by Melrose.⁶ When $\omega_g \rightarrow 0$ and when the electrons are monoenergetic, $G(\mu) = \delta(\mu - \mu_0)$, the interchange instability appears

with a real frequency $\omega = m\omega_{dh}(\mu_0)/2$ whenever the energetic electron pressure gradients exceed a threshold, $\Gamma_h^2(\mu_0) > m_\perp^2 \omega_{dh}^2/4$, as explained by Krall.¹⁷ When the distribution of energies has an exponential form, e.g., $G(\mu) \propto e^{-\mu/\mu_0}$, the integral in Eq. (5) can be expressed in terms of an exponential integral function, while making use of Landau's method to preserve causality for complex ω . This form best represents the experiment.

When the centrifugal drive is combined with a pressure drive from a distribution of energetic electrons, then the low azimuthal mode number m observed for the centrifugal interchange instability can be explained. With a low bias, the rotational drive is small, and HEI drive is, comparatively, larger. In this regime, low m modes are seen to be most unstable. As the bias increases, the rotational drive increases, and a regime where $m=2$ is most unstable is attained.

This interpretation is strengthened by the fact that the $m=2$ regime is only observed when the dipole magnet current is reduced. Lowering the B field has the combined effect of increasing the $\mathbf{E} \times \mathbf{B}$ frequency and thus the rotational instability drive, as well as moving the ECRH resonance location from inside the plasma volume onto the suspended terrella itself, thereby reducing α and the HEI drive. With the magnet power reduced to 70% (Fig. 4), application of large external bias resulted in a phasing out of the $m=1$ dominated regime and an emergence of an $m=2$ dominated one. In contrast, at 100% B (Fig. 3) only the strong $m=1$ regime is observed.

B. Nonlinear simulation

In addition to the linear theory, we have modified a nonlinear, self-consistent numerical simulation in order to interpret the observed rotational instabilities. This simulation is described fully elsewhere^{31,19} and reproduces the observed modes. The simulation explicitly solves for the evolution of cold ion and energetic electron number densities and the electrostatic potential Φ on the (ψ, ϕ) plane. (ψ, ϕ) are simultaneously the canonical coordinates of the electrons' guiding-center drift Hamiltonian (i.e., the electron phase space) and the magnetic coordinates of the dipole, $\mathbf{B} = \nabla\psi \times \nabla\phi$.³³ Plasma $\mathbf{E} \times \mathbf{B}$ drifts, ion polarization and centrifugal drifts, and energetic electron magnetic drifts determine particle dynamics, and Poisson's equation in magnetic coordinates determines the nonlinear evolution of the potential.

Since the plasma undergoes rigid rotation, the modification required to model the centrifugal interchange instability is easily implemented when the evolution equations are expressed in the plasma's rotating frame. In this frame, only the equation for cold ion dynamics changes. Using previous notation,^{31,19} the number of ions within a tube of unit flux, $N_i(\psi, \phi, t)$, evolves in time due to the net flux of ions caused by density-weighted, field-line averaged particle drifts,

$$\frac{\partial N_i}{\partial t} + \frac{\partial}{\partial \phi} \left[cN_i \left(\omega_g(\psi) - \frac{\partial \tilde{\Phi}}{\partial \psi} - \kappa_\phi \frac{\partial \dot{\tilde{\Phi}}}{\partial \phi} \right) \right] + \frac{\partial}{\partial \psi} \left[cN_i \left(\frac{\partial \tilde{\Phi}}{\partial \phi} - \kappa_\psi \frac{\partial \dot{\tilde{\Phi}}}{\partial \psi} \right) \right] = 0, \quad (6)$$

where $\omega_g(\psi) \approx -0.58\omega_E^2/\omega_{ci}^* \propto L^3$ is the net ion drift due to the centrifugal force. The centrifugal force varies along a field line and reverses sign as the field line approaches the magnetic poles. However, these variations are irrelevant for the electrostatic interchange mode. It evolves according to the motion of plasma contained within entire flux tubes, and the mode is an example of fluid dynamics in only two dimensions (ψ, ϕ) . The Coriolis correction is proportional to $\omega_E/\omega_{ci} \sim 0.03 \ll 1$ and can be ignored. The ion polarization terms are $\kappa_\phi \approx 0.66/(\omega_{ci}^*\psi)$ and $\kappa_\psi \approx 0.77\psi/\omega_{ci}^*$, where ω_{ci}^* is the ion cyclotron frequency at the equatorial plane of a field line.

Starting from a specified initial condition, the simulation explicitly solves for the time evolution of multiple, charged fluids (i.e., the ions and a collection of energetic electron populations) that are defined on a (ψ, ϕ) grid and interact nonlinearly through a perturbed electrostatic potential $\tilde{\Phi}$. The system is entirely closed (i.e., no particles are lost or added), and $\tilde{\Phi}$ vanishes at the surfaces of the vacuum vessel and the dipole magnet. Interchange stability is determined by the rotation rate ω_E , the fraction of energetic electrons $\alpha(\psi)$, and the initial plasma profile $N_i(\psi)$. Additionally, a small nonresonant dissipation is added to damp potential fluctuations. Dissipation is needed to explain the nonlinear phenomena of "frequency sweeping" that has been observed in CTX.^{31,19-21}

The initial conditions selected to model the observations reported here are similar to those reported previously¹⁹⁻²¹ except the energetic electron pressure was reduced, reflecting the effects of higher neutral gas pressures and reduced dipole field in the experiment. The average magnetic drift frequency of the energetic electron energy was halved, and the fraction of hot electrons, α , ranged from 5% to 20%.

The simulation produces a global mode dominated by low m numbers, characterized by dramatic ion mixing and a flattening of the ion density profile. With lower instability drive (lower rotation frequency) $m=1$ is seen to dominate but higher modes become larger with increasing rotation frequency. As the centrifugal drive ω_g increased and the energetic electron fraction decreased, the nature of the interchange mode changed significantly, similar to observation. For $\alpha \sim 0.05$ and rapid plasma rotation, $\omega_E/\omega_{dh} > 0.2$, the most unstable interchange mode has a shorter wavelength, $m=4$, and grows with nearly zero real frequency in the rotating frame. This mode represents the "ideal" rotational interchange⁶ with a linear growth rate γ given by $\gamma^2 \approx \omega_{ci}\omega_g d(\ln N_i)/d(\ln \psi)$. As the rotational drive is reduced or when the energetic electron population increases, the azimuthal mode number m decreases and the interchange mode acquires a real frequency in the direction of the electron magnetic drift. A localized linear theory of the interchange

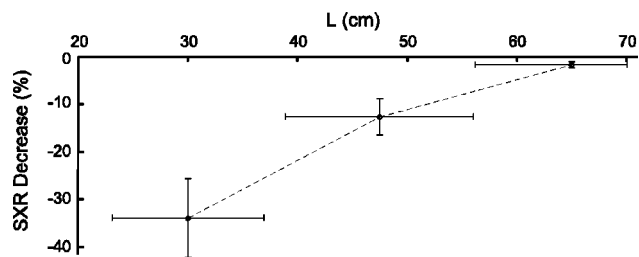


FIG. 10. Fractional decrease in the measured soft x-ray signals due to the external bias (-400 V) collimated at three different radial cords through the plasma.

mode interacting with a distribution of deeply trapped electrons shows the real frequency results from electron drift resonance³⁴ (see Sec. V A). When $\alpha=0.2$ and $\omega_E \approx 19$ kHz, the mode frequency is ≈ 7 kHz in the rotating frame, or 26 kHz in the lab frame, just as is experimentally observed in Fig. 4. As α increases further, the interchange mode rotates more quickly and the fastest growing mode is dominated by $m=1$. Figure 9 summarizes the computed interchange mode structures as a function of ω_E and α . The ion polarization currents induced by the real frequency also stabilizes higher m modes more strongly and, as such, is important in reproducing the unstable low m modes in the simulation.

In addition, the simulation reproduces the measured radial structures of the centrifugal interchange mode. This is shown in Fig. 6 by the solid lines superimposed with the correlation measurements. We believe the remarkably good agreement is a general consequence of solutions to Poisson's Equation that take into account the dielectric properties of plasma confined by a dipole magnetic field. This was first noted for the electron pressure-driven mode.¹⁹ Indeed, the broad mode structures of both the fast, $\omega \sim m\omega_{dh}$, energetic electron mode and the much slower, $\omega \sim m\omega_E$ (and lower amplitude), centrifugal mode are similar. The main difference is that the centrifugal mode is broader and has a "spiral" structure, characterized by the $\pi/2$ radial phase shift, reflecting its different source of field-line charging. This aspect of the structure is also captured by the simulation, shown by the solid lines in Fig. 7(b).

VI. COMMENT ON INTERCHANGE TRANSPORT

Though the interaction of the centrifugally driven interchange instability with energetic particles and its mode structure have been observed and well correlated with linear theory and simulation, the particle transport that must necessarily result from this mode has not been studied in depth. However, some evidence of transport has been observed through monitoring of the density profile.

To monitor the density profile close to the core of the plasma, soft x-ray measurements were taken, since material probes destructively interfere with the plasma. An array of three soft x-ray diodes focused on the inner, central, and outer plasma regions, respectively, measuring a flattening of the density profile in the presence of the bias relative to the case without the bias. This observation, Fig. 10, may represent interchange transport and density profile flattening. It is

interesting that the edge probe measurements in Fig. 2 do not show a profile change with equatorial bias. While these measurements suggest plasma transport, we have not yet been able to characterize this process fully.

VII. SUMMARY

In summary, we report the first experimental observations of the centrifugally driven interchange mode, excited in the CTX dipole-confined plasma by inducement of $\mathbf{E} \times \mathbf{B}$ rotation with application of a radial electric field. Electric fields are created using an equatorial mesh that protrudes into the plasma's inner most flux tubes and alters the plasma's equilibrium electrostatic potential with respect to the outer chamber wall. The radial current is consistent with ion-neutral transport, and rotation rates approaching sonic speeds are observed.

The mode structures for these instabilities are dominated by low azimuthal Fourier components and broad radial structures. The mode structures are measured using a correlation analysis of movable high-impedance floating potential probes located at various positions within the plasma as well as a novel polar imager array. These structures are reproduced by a fully self-consistent nonlinear particle simulation of interchange instabilities in dipole geometry. The dispersive properties of the global, coherent modes are modified by the presence of the hot electron population, which causes long wavelength modes to be more unstable: drift resonant particles induce polarization currents which preferentially stabilize higher m modes. Observations of both centrifugally driven interchanges as well as interchanges driven by hot electron pressure have been made simultaneously in the same discharge.

Although the plasma pressure in the CTX device is much less than found in the gas giant magnetospheres, we believe our observations of the centrifugal interchange instability may have relevance to the confinement and particle transport in those systems.

¹M. C. Kelly, *The Earth's Ionosphere* (Academic, New York, 1989).

²G. Bateman, *MHD Instabilities* (MIT, Cambridge, 1978).

³D. Meade, Phys. Rev. Lett. **17**, 677 (1966).

⁴F. J. Øynes, H. L. Pécseli, and K. Rypdal, Phys. Rev. Lett. **75**, 81 (1995).

⁵K. Rypdal, O. E. Garcia, and J.-V. Paulsen, Phys. Rev. Lett. **79**, 1857 (1997).

⁶D. B. Melrose, Planet. Space Sci. **15**, 381 (1967).

⁷C. T. Russel, Adv. Space Res. **33**, 2004 (2004).

⁸C. T. Russel, M. G. Kivelson, K. K. Khurana, and D. E. Huddleston, Adv. Space Res. **26**, 1671 (2004).

⁹M. G. Kivelson, K. K. Khurana, C. T. Russel, and R. J. Walker, Geophys. Res. Lett. **24**, 2127 (1997).

¹⁰R. M. Thorne *et al.*, Geophys. Res. Lett. **24**, 2131 (1997).

¹¹G. K. Siscoe and D. Summers, J. Geophys. Res. **86**, 8471 (1981).

¹²T. W. Hill, A. J. Dessler, and L. J. Maher, J. Geophys. Res. **86**, 9020 (1981).

¹³D. J. Southwood and M. G. Kivelson, J. Geophys. Res. **92**, 109 (1987).

¹⁴Y. S. Yang, R. A. Wolf, R. W. Spiro, T. W. Hill, and A. J. Dessler, J. Geophys. Res. **99**, 8755 (1994).

¹⁵K. M. Ferrière, C. Zimmer, and M. Blanc, J. Geophys. Res. **106**, 327 (2001).

¹⁶A. N. Fazakerly and D. J. Southwood, J. Geophys. Res. **97**, 10787 (1992).

¹⁷N. A. Krall, Phys. Fluids **9**, 820 (1966).

¹⁸H. L. Berk, Phys. Fluids **19**, 1255 (1976).

¹⁹H. P. Warren and M. E. Mauer, Phys. Rev. Lett. **74**, 1351 (1995).

²⁰H. P. Warren and M. E. Mauer, Phys. Plasmas **2**, 4185 (1995).

- ³⁰H. P. Warren, M. E. Mael, D. Brennan, and S. Taromina, *Phys. Plasmas* **3**, 2143 (1996).
- ³¹M. E. Mael, *J. Phys. IV* **7**, 307 (1997).
- ¹⁹B. Levitt, D. Maslovsky, and M. Mael, *Phys. Plasmas* **9**, 2507 (2002).
- ²⁰D. Maslovsky, B. Levitt, and M. E. Mael, *Phys. Rev. Lett.* **90**, 185001 (2003).
- ²¹D. Maslovsky, B. Levitt, and M. E. Mael, *Phys. Plasmas* **90**, 185001 (2003).
- ²²S. A. Balbus and J. F. Hawley, *Rev. Mod. Phys.* **70**, 1 (1998).
- ²³Y. Huang and A. B. Hassam, *Phys. Plasmas* **11**, 2459 (2004).
- ²⁴S. Chandrasekhar, *Hydrodynamic and Hydromagnetic Instability* (Oxford University Press, Oxford, 1961).
- ²⁵E. N. Parker, *Astrophys. J.* **145**, 811 (1966).
- ²⁶B. Lehnert, *Nucl. Fusion* **11**, 485 (1971).
- ²⁷A. B. Hassam, *Comments Plasma Phys. Controlled Fusion* **18**, 263 (1997).
- ³³A. H. Boozer, *Phys. Fluids* **23**, 904 (1980).
- ³⁴B. Levitt, Ph.D. dissertation, Columbia University, New York, 2004.
- ³²H. Saitoh, Z. Yoshiuda, H. Himura, J. Morikawa, and M. Fukao, *Phys. Plasmas* **11**, 3331 (2004).